Available online at www.sciencedirect.com
ScienceDirect
Journal of Computational Physics 227 (2007) 292–314
JOURNAL OF COMPUTATIONAL PHYSICS
www.elsevier.com/locate/jcp

A direct-forcing fictitious domain method for particulate flows

Zhaosheng Yu *, Xueming Shao

Department of Mechanics, State Key Laboratory of Fluid Power Transmission and Control, Zhejiang University, 310027 Hangzhou, China

Received 2 March 2007; received in revised form 26 July 2007; accepted 31 July 2007
Available online 10 August 2007

Abstract

A direct-forcing fictitious domain (DF/FD) method for the simulation of particulate flows is reported. The new method is a non-Lagrange-multiplier version of our previous DLM/FD code and is obtained by employing a discrete δ-function in the form of bi(tri-) function to transfer explicitly quantities between the Eulerian and Lagrangian nodes, as in the immersed boundary method. Due to the use of the collocation-point approach for the rigidity constraint and the integration over the particle domain, the Lagrangian nodes are retracted a little from the particle boundary. Our method in case of a prescribed velocity on the boundary is verified via the comparison to the benchmark results on the flow over a fixed cylinder in a wide channel and to our spectral-element results for a channel with the width of four cylinder diameters. We then verify our new method for the case of the particulate flows through various typical flow situations, including the sedimentation of a circular particle in a vertical channel, the sedimentation of a sphere in a vertical pipe, the inertial migration of a sphere in a circular Poiseuille flow, the behavior of a neutrally-buoyant sphere in Couette flow, and the rotation of a prolate spheroid in Couette flow. The accuracy and robustness of the new method are fully demonstrated, in particular for the case of relatively low Reynolds numbers and the neutrally-buoyant case.

Keywords: Direct-forcing; Fictitious domain method; Particulate flows; Immersed boundary; Lagrange multiplier

1. Introduction

The non-boundary-fitted (or Cartesian grid) method has become increasingly popular for the solution of the fluid flow problems in a complex geometry or with moving boundaries. A variety of non-boundary-fitted approaches have been developed, and they can be roughly classified into two families [1,2]: the body-force based method (e.g., [3–13]) and the non-body-force based method (e.g., [2,14–17]). For the former, a body-force (or momentum forcing) is introduced into the momentum equation. The fractional step scheme is often used in the body-force based methods to simplify the computation in the following way: the Navier–Stokes equations are solved for the known body-force obtained at the previous time level, with the boundary condition on the immersed boundary disregarded, and subsequently the boundary condition is used to determine

* Corresponding author. Tel.: +86 13777455377.
E-mail address: yuzhaosheng@zju.edu.cn (Z. Yu).

0021-9991/$ - see front matter
doi:10.1016/j.jcp.2007.07.027

the body-force. There exist various body-force based methods in the literature that differ in the way the body-force is calculated. For example, for the Lagrange-multiplier based fictitious domain method (e.g. [3–7]), the body-force is introduced as a Lagrange multiplier in a weak formulation, and solved from the boundary condition in an iterative way. For the elastic-force based immersed boundary method (e.g., [8–10]), the boundary (or the body) moves with the local fluid and the body-force is explicitly calculated from the displacement or deformation of the boundary (large stiffness constant as an approximation to the rigid-boundary problems). For the direct-forcing based immersed boundary method (e.g. [11–13]), the body-force is computed explicitly from the boundary condition in two typical manners: for one [11], the body-force is defined at the Lagrangian points on the boundary, and a discrete δ-function is used to interpolate the fluid velocity from the Eulerian nodes to the Lagrangian nodes for the calculation of the body-force and then to distribute the body-force from the Lagrangian nodes to the Eulerian nodes for the solution of the fluid momentum equation; for the other, the body-force is directly defined at the Eulerian nodes located in the immediate vicinity of the boundary in either the real fluid region [12] or the fictitious domain [13] (thus there is no need for the transfer of the body-force), and the target velocities at the forcing points for the calculation of the body-force is obtained by interpolation of the prescribed velocity at the boundary and other fluid velocities at the Eulerian nodes. Unlike the body-force based method, the non-body-force based method does not introduce a body-force, instead, it accounts for the boundary condition by either transforming it into independent equations [14] or using it to modify the expressions of differential operators for the Eulerian nodes in the immediate vicinity of the boundary ([15–17]). One advantage of the non-body-force based method is that the jump boundary conditions on the surface can be conveniently handled.

We are concerned with the simulation of particulate flows (fluid–structure interactions) in the present study. In principle, all aforementioned methods can be applied to the particulate flows, however, the body-force based method has been predominantly used so far. A common feature for the body-force based method is that the hydrodynamic force on the particles can be calculated from the body-force and is not necessary to be explicitly computed in order to determine the particle velocities. For the distributed-Lagrange-multiplier/fictitious-domain (DLM/FD) method proposed by Glowinski et al. [5], the particle velocities and the body-force (Lagrange multiplier) are solved together with the implicit scheme, while for the immersed boundary method (e.g., [11–13]), they are obtained explicitly. The DLM/FD method has been successfully applied to a wide range of particulate flow problems (e.g., [6,18–22]). However, its calculation of the particle velocity and body-force is a little more involved and expensive compared to the direct-forcing immersed boundary (DF/IB) method. The aim of the present study is to present a non-Lagrange-multiplier version of our previous DLM/FD code without sacrificing the accuracy and robustness by employing a discrete δ-function in the form of bi(tri-) function to transfer explicitly quantities between the Eulerian and Lagrangian nodes, as in the immersed boundary method. In our previous DLM/FD code, the bi(tri)-linear function is actually already used to interpolate the quantities from the Eulerian nodes to the Lagrangian nodes and to distribute the body-force from the Lagrangian nodes to the Eulerian nodes, however, it is not defined as a discrete δ-function to explicitly transfer (or equate) the quantities between the two frames, and therefore the body-force needs to be determined implicitly from the constraint of the velocities in the two frames being equal in the solid domain or on the boundary. For convenience, we refer to our new method as direct-forcing fictitious domain (DF/FD) method, since on one hand it is resulted from a modification over our previous DLM/FD code and on the other hand it deals with the body-force in essentially the same way as the DF/IB method. Compared to the DF/IB method for the particulate flows proposed by Uhlmann [11], in which the body-force is only distributed on the particle boundary, our body-force is distributed over the particle inner domain for the constraint that all inner fluids move as a rigid-body so that the time acceleration term of the inner fluids involved in the calculation of the hydrodynamic torque on the particles does not need to be calculated explicitly, thus circumventing the difficulty in dealing with the nearly neutrally-buoyant case in [11]. We note that other non-Lagrange-multiplier versions of the FD method have been developed by Sharma and Patankar [23] and Veeramani et al. [24]. Compared to these two methods, our method has the same feature that the constraint of the rigid-body motion for the inner fluids is used to derive an explicit expression for the particle velocities, but the form of the explicit expression and the computational schemes used are different.

The rest of the paper is organized as follows: we describe the new scheme for the explicit solution of the particle velocities and the body-force in detail in the following section. In Section 3, we first validate the

method in case of prescribed velocity on the immersed boundary via the benchmark problem of the flow over a fixed cylinder, and it is shown that for the case of the singular body-force distributed only on the boundary the discrete nominal support area for the body-force is not important to the results and the Lagrangian nodes should be retracted a little from the boundary if one wants to use the body-force to calculate the hydrodynamic force on the body. We then verify our new method for the case of the particulate flows through various typical flow situations, including the sedimentation of a circular particle in a vertical channel, the sedimentation of a sphere in a vertical pipe, the inertial migration of a sphere in circular Poiseuille flow, the behavior of a neutrally-buoyant sphere in Couette flow, and the rotation of a prolate spheroid in Couette flow. Concluding remarks are given in the final section.

2. Numerical model

The method proposed in the present study is an improved version of our DLM/FD code, and only differs in that the Lagrange multiplier (i.e., body-force or momentum forcing) and particle velocities are solved in a non-iterative way. Hence, the description of the new algorithm can be started from the DLM/FD formulation proposed by Glowinski et al. [5]. However, we will derive the new algorithm directly from the primitive governing equations, since such a derivation is straightforward and can make the entire algorithm involve less mathematics by getting rid of the concept of weak formulation.

For simplicity of description, only one particle is considered. Let $P(t)$ and $\partial P(t)$ represent the solid domain and its boundary, Ω_f the real fluid region, and Ω the entire domain comprising both interior and exterior of the body.

2.1. Fictitious domain formulation

The momentum equation for the fluid flow is

$$\rho_f \frac{\mathrm{d}\mathbf{u}}{\mathrm{d}t} = \nabla \cdot \boldsymbol{\sigma} \quad \text{in } \Omega_f, \tag{1}$$

where ρ_f is the fluid density, $\mathbf{u}$ the fluid velocity, and $\boldsymbol{\sigma}$ the fluid stress. Only the Newtonian fluid is considered in this study, thus $\boldsymbol{\sigma} = -p\mathbf{I} + 2\mu\mathbf{D}$, here p being the fluid pressure, μ the viscosity and $\mathbf{D}$ the rate-of-strain tensor.

The motion of the rigid particle is governed by Newton's equation of motion as follows:

$$M\frac{\mathrm{d}\mathbf{U}}{\mathrm{d}t} = \mathbf{F}^{\mathrm{H}} + \left(1 - \frac{1}{\rho_{\mathrm{r}}}\right)M\mathbf{g}, \tag{2}$$

$$\frac{\mathrm{d}(\mathbf{J}\cdot\boldsymbol{\omega}_s)}{\mathrm{d}t} = \mathbf{T}^{\mathrm{H}}, \tag{3}$$

where M, $\mathbf{J}$, U, and $\boldsymbol{\omega}_s$ are the particle mass, moment of inertia tensor, translational velocity and angular velocity, respectively. $\mathbf{g}$ is the gravitational acceleration, and ρ_{r} is the solid–fluid density ratio. $\mathbf{F}^{\mathrm{H}}$ and $\mathbf{T}^{\mathrm{H}}$ are the hydrodynamic force and torque on the particle, respectively, defined by

$$\mathbf{F}^{\mathrm{H}} = \int_{\partial P} \mathbf{n}\cdot\boldsymbol{\sigma}\,\mathrm{d}s, \tag{4}$$

$$\mathbf{T}^{\mathrm{H}} = \int_{\partial P} \mathbf{r}\times(\mathbf{n}\cdot\boldsymbol{\sigma})\mathrm{d}s, \tag{5}$$

where $\mathbf{n}$ is the unit outward normal on the particle surface and $\mathbf{r}$ is the position vector with respect to the particle mass center. Note that the gravity term is not considered in (1), which has no effect on the flow, but can produces a hydrostatic pressure and thereby a buoyance force on the particle. Since the buoyance force is not included in $\mathbf{F}^{\mathrm{H}}$, we need to include it directly in (2).

As in the DLM/FD method, the interior of the particle is filled with the fluid and a pseudo body-force is introduced over the particle inner domain to enforce the fictitious fluid to satisfy the rigid-body motion constraint, namely, the following equations are introduced for the interior of the particle:

$$\rho_f \frac{\mathrm{d}\mathbf{u}}{\mathrm{d}t} = \nabla \cdot \boldsymbol{\sigma} + \boldsymbol{\lambda} \quad \text{in } P(t), \tag{6}$$

$$\mathbf{u} = \mathbf{U} + \boldsymbol{\omega}_s \times \mathbf{r} \quad \text{in } P(t), \tag{7}$$

where $\boldsymbol{\lambda}$ is the pseudo body-force. Integrating (6) and $\mathbf{r}\times$(6) over the particle interior $P(t)$ and substituting into Eqs. (4), (5) and (7) yields, respectively,

$$\mathbf{F}^H = -\int_P \boldsymbol{\lambda}\,\mathrm{d}\mathbf{x} + \frac{M}{\rho_\mathrm{r}}\frac{\mathrm{d}\mathbf{U}}{\mathrm{d}t}, \tag{8}$$

and

$$\mathbf{T}^\mathrm{H} = -\int_P \mathbf{r}\times\boldsymbol{\lambda}\mathrm{d}\mathbf{x} + \frac{1}{\rho_\mathrm{r}}\frac{\mathrm{d}(\mathbf{J}\cdot\boldsymbol{\omega}_s)}{\mathrm{d}t}. \tag{9}$$

Substituting (8) into (2), and (9) into (3) gives, respectively,

$$\left(1-\frac{1}{\rho_\mathrm{r}}\right)M\left(\frac{\mathrm{d}\mathbf{U}}{\mathrm{d}t}-\mathbf{g}\right) = -\int_P \boldsymbol{\lambda}\,\mathrm{d}\mathbf{x}, \tag{10}$$

$$\left(1-\frac{1}{\rho_\mathrm{r}}\right)\frac{\mathrm{d}(\mathbf{J}\cdot\boldsymbol{\omega}_s)}{\mathrm{d}t} = -\int_P \mathbf{r}\times\boldsymbol{\lambda}\,\mathrm{d}\mathbf{x}. \tag{11}$$

We see that (1), (6), (7), (10) and (11) are simply the strong-form counterparts of the DLM/FD combined momentum equations in the weak form derived by Glowinski et al. We also note that Diaz-Goano et al. [25] have conducted a similar derivation and obtained essentially the same formulation as above.

The governing equations can be non-dimensionlized by introducing the following scales: L_c for length, U_c for velocity, L_c/U_c for time, $\rho_f U_c^2$ for the pressure p and $\rho_f U_c^2/L_c$ for the pseudo body-force. For convenience, we write the dimensionless quantities in the same form as their dimensional counterparts, unless otherwise specified. The dimensionless equations for the incompressible fluid can be written as follows:

$$\frac{\partial\mathbf{u}}{\partial t} + \mathbf{u}\cdot\nabla\mathbf{u} = \frac{\nabla^2\mathbf{u}}{Re} - \nabla p + \boldsymbol{\lambda} \quad \text{in } \Omega, \tag{12}$$

$$\mathbf{u} = \mathbf{U} + \boldsymbol{\omega}_s \times \mathbf{r} \quad \text{in } P(t), \tag{13}$$

$$\nabla\cdot\mathbf{u} = 0 \quad \text{in } \Omega, \tag{14}$$

$$(\rho_\mathrm{r}-1)V_\mathrm{p}^*\left(\frac{\mathrm{d}\mathbf{U}}{\mathrm{d}t} - Fr\frac{\mathbf{g}}{g}\right) = -\int_P \boldsymbol{\lambda}\,\mathrm{d}\mathbf{x}, \tag{15}$$

$$(\rho_\mathrm{r}-1)\frac{\mathrm{d}(\mathbf{J}^*\cdot\boldsymbol{\omega}_s)}{\mathrm{d}} = -\int_P \mathbf{r}\times\boldsymbol{\lambda}\,\mathrm{d}\mathbf{x}. \tag{16}$$

In the above equations, Re represents the Reynolds number defined by $Re = \frac{\rho_f U_c L_c}{\mu}$, Fr the Froude number defined by $Fr = \frac{gL_c}{U_c^2}$, V_p^* the dimensionless particle volume define by $V_\mathrm{p}^* = \frac{M}{\rho_s L_c^d}$, and $\mathbf{J}^*$ the dimensionless moment of inertia tensor defined by $\mathbf{J}^* = \frac{\mathbf{J}}{\rho_s L_c^{d+2}}$, here ρ_s being the particle density and d being the dimensionality of the problem involved. Note that the pseudo body-force $\boldsymbol{\lambda}$ in (12) is defined in the solid domain $P(t)$.

2.2. Direct forcing scheme

2.2.1. Fractional-step time scheme

As in the DLM/FD method, a fractional-step time scheme is used to decouple the combined system (12)–(16) into two subproblems:

Fluid subproblem for $\mathbf{u}^*$ and p:

$$\frac{\mathbf{u}^*-\mathbf{u}^n}{\Delta t} - \frac{\nabla^2\mathbf{u}^*}{2Re} = -\nabla p - \frac{1}{2}[3(\mathbf{u}\cdot\nabla\mathbf{u})^n - (\mathbf{u}\cdot\nabla\mathbf{u})^{n-1}] + \frac{\nabla^2\mathbf{u}^n}{2Re} + \boldsymbol{\lambda}^n, \tag{17}$$

$$\nabla\cdot\mathbf{u}^* = 0. \tag{18}$$

Particle subproblem for $\mathbf{U}^{n+1}$, $\boldsymbol{\omega}^{n+1}$, $\mathbf{u}^{n+1}$ and $\boldsymbol{\lambda}^{n+1}$:

$$\frac{\mathbf{u}^{n+1}-\mathbf{u}^{*}}{\Delta t}=\boldsymbol{\lambda}^{n+1}-\boldsymbol{\lambda}^{n}, \tag{19}$$

$$\mathbf{u}^{n+1}=\mathbf{U}^{n+1}+\boldsymbol{\omega}_s^{n+1}\times\mathbf{r}, \tag{20}$$

$$(\rho_{\mathrm{r}}-1)V_{\mathrm{p}}^{*}\left(\frac{\mathbf{U}^{n+1}-\mathbf{U}^{n}}{\Delta t}-Fr\frac{\mathbf{g}}{g}\right)=-\int_P\boldsymbol{\lambda}^{n+1}\,\mathrm{d}\mathbf{x}, \tag{21}$$

$$(\rho_{\mathrm{r}}-1)\left[\frac{\mathbf{J}^{*}\cdot(\boldsymbol{\omega}_s^{n+1}-\boldsymbol{\omega}_s^{n})}{\Delta t}+\boldsymbol{\omega}_s^{n}\times(\mathbf{J}^{*}\cdot\omega_s^{n})\right]=-\int_P\mathbf{r}\times\boldsymbol{\lambda}^{n+1}\,\mathrm{d}\mathbf{x}. \tag{22}$$

The fluid subproblem (17)–(18) is a standard Navier–Stokes problem. The reader is referred to [7] (for 2D) and [21] (for 3D) for the detailed description of our solver, a finite-difference-based projection method on a half-staggered grid. The resulting Poisson equation for the pressure is solved with a FFT based fast solver.

2.2.2. Solution of the particle subproblem

The difficulty in the particle problem (19)–(22) comes from the fact that the fluid velocity is defined at the structured Eulerian nodes, whereas the surface of the particle needs to be described with the Lagrangian nodes that normally does not coincide with the Eulerian nodes, and consequently it is not straightforward how to solve the equations involving both Eulerian and Lagrangian quantities such as (19) and (20). In the previous DLM/FD works (e.g., [5,21]), the particle problem (19)–(22) is formulated in a weak form and then becomes a saddle-point problem, which is solved with Uzawa iteration. The δ-function is often used to discretize the Lagrange multiplier, resulting in the collocation-point method to enforce the rigidity constraint (or Dirichlet boundary condition) (e.g., [4,5]). In fact, if we use the δ-function to transfer a quantity between the Eulerian and Lagrangian frames explicitly as in the immersed boundary method, a non-iterative scheme for the solution of (19)–(22) can be easily devised. In the present study, we adopt the linear function (bi-linear for 2D and tri-linear for 3D) as a discrete approximation to the δ-function. For the case of 3D, the discrete δ-function is defined by

$$\delta_h(\mathbf{r})=d_h(\mathbf{r}_x)\cdot d_h(\mathbf{r}_y)\cdot d_h(\mathbf{r}_z), \tag{23}$$

where $\mathbf{r}_x$, $\mathbf{r}_y$ and $\mathbf{r}_z$ denote the components of $\mathbf{r}$, and $d_h(r)$ is defined by

$$d_h(r)=\begin{cases}1-\left|\frac{r}{h}\right| & \text{for } |r|<h,\\ 0 & \text{otherwise,}\end{cases} \tag{24}$$

in which h is the mesh-size of the homogeneous Eulerian (or Cartesian) grid. Using the discrete δ-function, we can transfer a discrete quantity f between the Eulerian ($\mathbf{x}_i$) and Lagrangian ($\mathbf{X}_l$) frames as follows:

$$f_{\mathrm{E}\to\mathrm{L}}: f_L(\mathbf{X}_l)=\sum_i f_E(\mathbf{x}_i)\delta_h(\mathbf{x}_i-\mathbf{X}_l), \tag{25}$$

$$f_{\mathrm{L}\to\mathrm{E}}: f_E(\mathbf{x}_i)=\sum_l f_L(\mathbf{X}_l)\delta_h(\mathbf{x}_i-\mathbf{X}_l)\Delta V_l^{*}, \tag{26}$$

where $f_{\mathrm{E}}(\mathbf{x}_i)$ and $f_{\mathrm{L}}(\mathbf{X}_l)$ represent the values of f at the Eulerian nodes $\mathbf{x}_i$ and at the Lagrangian nodes $\mathbf{X}_l$, respectively, and ΔV_l^{*} is the ratio of the size of the control volume for each Lagrangian node (ΔV_l) to h^d, d being the dimensionality. In the present study, for the case of f being defined throughout the body $P(t)$, we use the rectangular rule for the integration and assume that each Lagrangian node has the same integration volume, so that $\Delta V_l=\frac{V_{\mathrm{P}}^{*}}{N}$, N being the number of the Lagrangian nodes for $P(t)$. For the case of f being defined at the immersed boundary, it will be shown in our numerical test that V_l can be set to be an arbitrary value as long as it is not too large to cause instability; ΔV_l^{*} being unity is a good choice, irrespective of the distance between the Lagrangian nodes.

In the following, we first derive an explicit expression for $\mathbf{U}^{n+1}$ and $\boldsymbol{\omega}^{n+1}$ under the assumption that a quantity can be transferred between the Eulerian and Lagrangian frames accurately (or we consider quantities in a non-discretized space). Substituting (20) into (19) yields

$$\frac{\mathbf{U}^{n+1}+\boldsymbol{\omega}_s^{n+1}\times\mathbf{r}-\mathbf{u}^*}{\Delta t}=\boldsymbol{\lambda}^{n+1}-\boldsymbol{\lambda}^n. \tag{27}$$

Adding $\int_P$(27)dx to (21), and $\int_P \mathbf{r}\times$ (27)dx to (22) gives, respectively,

$$\rho_r V_p^* \frac{\mathbf{U}^{n+1}}{\Delta t}=(\rho_r-1)V_p^*\left(\frac{\mathbf{U}^n}{\Delta t}-Fr\frac{\mathbf{g}}{g}\right)+\int_P\left(\frac{\mathbf{u}^*}{\Delta t}-\boldsymbol{\lambda}^n\right)\mathrm{d}\mathbf{x}, \tag{28}$$

$$\rho_r \frac{\mathbf{J}^*\cdot\boldsymbol{\omega}^{n+1}}{\Delta t}=(\rho_r-1)\left[\frac{\mathbf{J}^*\cdot\boldsymbol{\omega}_s^n}{\Delta t}-\boldsymbol{\omega}_s^n\times(\mathbf{J}^*\cdot\omega_s^n)\right]+\int_P\mathbf{r}\times\left(\frac{\mathbf{u}^*}{\Delta t}-\boldsymbol{\lambda}^n\right)\mathrm{d}\mathbf{x}. \tag{29}$$

All the right-hand side terms of (28) and (29) are known quantities, so $\mathbf{U}^{n+1}$ and $\boldsymbol{\omega}^{n+1}$ are obtained without iteration. The integration for the last terms in the above equations is performed using the values at the Lagrangian nodes as follows:

$$\int_P f\,\mathrm{d}\mathbf{x}=\sum_l f_L(\mathbf{X}_l)\Delta V_l=\frac{V_P^*}{N}\sum_l f_L(\mathbf{X}_l). \tag{30}$$

Then, $\boldsymbol{\lambda}^{n+1}$ defined at the Lagrangian nodes can be determined from (27):

$$\boldsymbol{\lambda}^{n+1}=\frac{\mathbf{U}^{n+1}+\boldsymbol{\omega}_s^{n+1}\times\mathbf{r}-\mathbf{u}^*}{\Delta t}+\boldsymbol{\lambda}^n. \tag{31}$$

Finally, the fluid velocities $\mathbf{u}^{n+1}$ at the Eulerian nodes are determined from (19):

$$\mathbf{u}^{n+1}=\mathbf{u}^*+\Delta t(\boldsymbol{\lambda}^{n+1}-\boldsymbol{\lambda}^n)_{\mathrm{L}\to\mathrm{E}} \tag{32}$$

Note that the fluid velocity $\mathbf{u}$ is defined at the Eulerian nodes, and the pseudo body-force $\boldsymbol{\lambda}$ is defined at the Lagrangian nodes. Hence, $\mathbf{u}^*$ in (28), (29) and (31) need to be interpolated from the Eulerian nodes to the Lagrangian nodes using (25), and the pseudo body-force in (32) to be distributed from the Lagrangian nodes to the Eulerian nodes using (26), as marked in (32) with the subscript.

It should be noted that similar explicit expressions for the particle velocities have been derived early by Glowinski et al. [6] from an approximation to the DLM/FD formulation (based on essentially the same assumption as the above) in order to avoid the singularity at $\rho_r=1$ in the DLM/FD formulation, but the authors claimed that the results from such an explicit calculation are of worse quality compared to those from the iterative scheme and thus did not present a complete description of the new approach. The same approximation has also been used by Yu [26] in his work on the DLM/FD method for fluid/flexible-body interactions, followed by Shi and Phan-Thien [27]. Eq. (28) is a reduced form of Eq. (54) in Yu [26] in the limiting case of rigid-body motion.

In case of a prescribed velocity on the boundary, the step (28) and (29) for the calculation of the particle velocities is not necessary and we start from the second step (31) for the calculation the body-force with the particle velocity term ($\mathbf{U}^{n+1}+\boldsymbol{\omega}_s^{n+1}\times\mathbf{r}$) replaced by the prescribed velocity $\mathbf{u}_0$. Substituting the modified (31) into (17) yields

$$\boldsymbol{\lambda}^{n+1}=\frac{\mathbf{u}_0-\mathbf{u}^n}{\Delta t}-\left[-\frac{1}{2}[3(\mathbf{u}\cdot\nabla\mathbf{u})^n-(\mathbf{u}\cdot\nabla\mathbf{u})^{n-1}]+\frac{(\nabla^2\mathbf{u}^*+\nabla^2\mathbf{u}^n)}{2Re}-\nabla p\right],$$

which is essentially the same as the direct-forcing formulation for the calculation of the body-force ([11–13]), the reason why we refer to our new method as DF/FD method.

One may set $\boldsymbol{\lambda}^n$ in (17) and (19) to be zero, as in Glowinski et al., but it has been shown that the presence of this term is helpful to reduce the error in the steady solution and allows one to use a significantly larger time step for low Reynolds number flows [21].

2.2.3. Why bi(tri-) linear function and collocation-point approach?

Two new issues occur when the new scheme (28)–(32) is used as a substitute for the Uzawa iteration in the original DLM/FD method: what discrete δ-function is better chosen to transfer the quantities between the two frames, and how to calculate the integral terms in (28) and (29)? We have already given our answers in the description of the new scheme earlier: bi(tri-) linear function and collocation-point method (using the

rectangular rule with the same integration volume for each Lagrangian node). Two forms for the discrete δ-function have been widely used: Peskin's discrete δ-function [28,11] and bi(tri-) linear function [10,29,30]. The reasons why we choose the bi-(tri-) linear function rather than Peskin's discrete δ-function are:

1. *For convenience*. The bi(tri-) linear function has been used in our DLM/FD code, and it is particularly suited to the case of particulate flows, since the particles often move close to the wall, with certain Lagrangian nodes being located within one Eulerian mesh from the wall, in which case no special treatment is required for the linear interpolation function.
2. *For less computational cost*. Clearly, linear interpolation function is computationally cheaper than Peskin's high-order interpolation function.
3. *For accuracy*. Compared to Peskin's 3-point or 4-point discrete δ-function [28], 2-point linear function is more compact. Accordingly, less overestimation in the drag force on the particle is observed in our numerical tests for the linear function if the Lagrangian nodes are not retracted from the boundary, or a smaller retraction distance is required to obtain a correct drag force for the linear function.

The role of the discrete δ-function is to transfer the quantities between the Lagrangian and Eulerian nodes. Peskin's discrete δ-function was derived from an analogue to the analytical δ-function and originally used to deal with the case of the quantities being defined on the volumeless boundary. For the case of the quantities being defined over a domain, the discrete δ-function actually serves as a mutual interpolation function. It is clear that the linear interpolation function works well for the interpolation of the quantities from the homogeneously distributed Eulerian nodes to the Lagrangian nodes, but not clear if it can work for the interpolation from the inhomogeneously distributed Lagrangian nodes to the Eulerian nodes. Suppose that a quantity is unity for all Lagrangian nodes in an infinitely large domain, then an ideal discrete δ-function is expected to produce the value of unity for each Eulerian node. For simplicity, we inspect the case of 1D and the Lagrangian nodes being homogeneously distributed. Assume that the spacing for the Eulerian and Lagrangian nodes is h and $h(1+\xi)$, respectively, and at point '0', the Eulerian and Lagrangian nodes coincide with each other. Then, from (26), we obtain the Eulerian value of $(1+\xi)$ at point '0', $(1-\xi^2)$ at points '1' to '$1/\xi$', and $(1+\xi)$ again at point '$1/\xi+1$', another coincident point. It can be easily verified that the average value of the obtained Eulerian quantity is unity, being equal to the Lagrangian one, however, the oscillation of the Eulerian values is obvious, which is severe if ξ is not small. Note that such an oscillation occurs for the case of the homogeneously distributed Lagrangian nodes. In fact, it is normally impossible to homogeneously distribute the nodes over a body with curved boundaries. If one assumes the same integration volume for each Lagrangian node, as in the present study, it is clear that the Eulerian values are larger at the places where the distribution density of the Lagrangian nodes is higher and smaller where the distribution density is lower, resulting in an oscillation again. This second type of oscillation can be alleviated if the individual different integration volume for each Lagrangian node is taken into account, but is difficult to remove due to the inherent difficulty in messless interpolation, for any discrete δ-function, whether Peskin's or linear function.

The above analysis shows the shortcoming of the bi(tri-) linear function as a discrete δ-function: it cannot transfer the quantities from the Lagrangian nodes to the Eulerian nodes smoothly. Indeed, when we directly used the bi-linear function to transfer the Lagrangian velocity $\mathbf{U}^{n+1}+\boldsymbol{\omega}_s^{n+1}\times\mathbf{r}$ to the Eulerian velocity $\mathbf{u}^{n+1}$, instead of (32), we found that the code broke down after running only a few time steps. Then why does (32) work? Substituting (31) into (32) yields

$$\mathbf{u}_{\mathrm{E}}^{n+1}=(\mathbf{U}^{n+1}+\boldsymbol{\omega}_s^{n+1}\times\mathbf{r})_{\mathrm{L}\to\mathrm{E}}-(\mathbf{u}^{*}_{\mathrm{E}\to\mathrm{L}\to\mathrm{E}}-\mathbf{u}^{*}_{\mathrm{E}}). \tag{33}$$

We see that there exists a correction term $(\mathbf{u}^{*}_{\mathrm{E}\to\mathrm{L}\to\mathrm{E}}-\mathbf{u}^{*}_{\mathrm{E}})$, which effectively cancels the oscillation in the $(\mathbf{U}^{n+1}+\boldsymbol{\omega}_s^{n+1}\times\mathbf{r})_{\mathrm{L}\to\mathrm{E}}$ and results in a smooth solution $\mathbf{u}^{n+1}$ in the solid domain, due to the fact that $\mathbf{u}^{*}$ is close to $\mathbf{u}^{n+1}$ with the difference of $O(\Delta t)$ (being equal to each other at steady state), as seen from (32).

The collocation-point approach has been widely used in the DLM/FD method (e.g., [4,5,19]). In this approach, the constraint of the rigid-body motion is enforced for each collocation point, and accordingly the Lagrangian multiplier (body-force) is also defined on the collocation points and determined from the rigidity constraint. For the present DF/FD method, we employ the same approach for the rigidity constraint. In addition, the collocation (i.e., Lagrangian) points are not only used for the rigidity constraint, but also for

the discretization of integrals over the interior of the particle. It has been shown that in the collocation-point approach, the collocation points need to be retracted slightly from the particle surface to avoid the overestimation of the hydrodynamic drag on the particle [10,21]. This overestimation was explained by the fact that the collocation points on the particle surface affect the fluid velocities outside the particle and thus effectively increase the particle size [10]. Not surprisingly, the retraction of the Lagrangian points from the particle surface is found also necessary for the present DF/FD method. Moreover, this retraction is now further required by the accurate integration with the rectangular rule: the optimal integration point for an element is normally not located on the element boundary, but inside the boundary. In addition, the retraction of the nodes can be an approach to improve the prediction of the particle velocity in case of a coarse mesh, as commonly used in the lattice-Boltzmann method [31]. Note that the retraction is required by the collocation-point approach, but is not necessary for the collocation-element method [7,21] or other specific integration procedures [24].

Besides the collocation-point approach, we have tested an alternative integration method in the problem of the sedimentation of a circular particle: we mesh the solid domain and then perform the integration for all integrals over the solid domain using the trapezoidal rule. Such a method (meshing and trapezoidal rule) is definitely more accurate than the collocation-point method (meshless and rectangular rule) for the integration alone, but we observed a more appreciable spurious oscillation with time in the terminal particle settling velocity (whatever the form of δ-function) compared to the results (Fig. 4) obtained using the collocation-point method with the node arrangement shown in Fig. 1b. A possible reason is that the Lagrangian nodes in the meshing method are not distributed as uniformly as in the meshless method, and the distribution homogeneity of the points influences significantly the quality of the solution through the discrete δ-function and the number of nodes which are smaller for a given h in case of the meshing method.

The particle volume V_p^* and moment of inertia tensor J^* in (28) and (29) can be given as either analytical (real) values or evaluated using the numerical integration (30). There is no difference between the calculated and analytical particle volumes, since the integration volume for each node ΔV_l is given from the real particle volume. There is slight difference for J^*, but our numerical experiments indicate that the effect of the different choice of J^* on the stability and accuracy of the method is negligibly small.

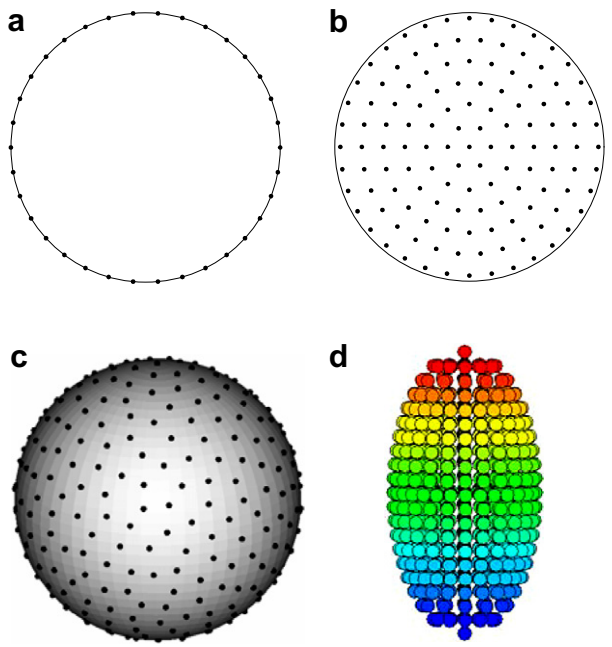

Fig. 1. Arrangements of Lagrangian points in cases of (a) a 2D cylinder with the no-slip condition enforced only on the boundary, (b) a circular particle, (c) a spherical particle (only the points on one layer is shown), and (d) a prolate spheroid.

2.2.4. Arrangement of the Lagrangian nodes

The validation tests in the present study involve the circular, spherical and spheroidal particles. Fig. 1 shows the arrangement patterns for the Lagrangian points for all cases studied. We attempt to distribute the points as homogeneously as possible. For the DLM/FD method, it is better for the spacing of the Lagrangian nodes to be slightly bigger than that of the Eulerian nodes for the sake of both accuracy and robustness, as suggested by Glowinksi et al. [5]. This guideline is adopted in the present DF/FD method.

For the circular particle, it is straightforward to distribute the nodes uniformly on the particle boundary as shown in Fig. 1a, which will be used for the simulation of the flow over a fixed cylinder. Let γ denote the relative distance between the nodes with respect to h, and then the number of the Lagrangian points is set by $N = \left[\frac{2\pi a}{\gamma h}\right]$, here a representing the particle radius, and the bracket '[ ]' the operator of taking the integer part. We typically set $\gamma = 1.45$, in order to avoid the possibility that there are two collocation nodes in a Cartesian cell.

For the case of the rigid-body motion constraint being enforced throughout the body of a circular particle, we distribute the collocation points on the concentric rings as shown in Fig. 1b: one point at the particle center, and $6i$ points on the ith ring for $i = 1, N_a$, N_a being the number of the rings. Thus the total number of the collocation points is $N = 1 + 3N_a(N_a + 1)$. For $h = a/8$, we find that $N_a = 6$ is a good choice. As mentioned earlier, the outmost ring needs to be retracted slightly from the particle boundary. Let Δa denote the retraction distance. Numerical tests show that $\Delta a = h/3$ is a good choice, in particular for the low Reynolds numbers. The optimal Δa is case-dependent, typically ranging from $h/4$ to $h/2$ except for a high Re. We note that the concentric arrangement of the nodes used here has been independently proposed by Yu et al. [19] and Uhlmann [32].

For the spherical particle, the Lagrangian nodes are distributed on the concentric spherical surfaces. On each surface, the distribution of the nodes is determined using the method suggested by Uhlmann [11]: let a certain number of point-particles that are confined to the spherical surface move under a mutual repulsive force which is proportional to the inverse of the square of the inter-particle distance, till the equilibrium configuration is achieved. The number of the collocation points on ith surface is set to be $N_b i^2$, here N_b being the number of nodes on the first surface from the particle center. Let N_a denote the number of the surfaces, and then the total number of the collocation nodes for a sphere is $N = 1 + N_b N_a(N_a + 1)(2N_a + 1)/6$. The distribution of 360 nodes on one surface ($N_b = 10$, $i = 6$) is shown in Fig. 1c. We suggest $N_a = \left[\frac{a}{h} - 0.5\right]$, $N_b = 8$ and $\Delta a = h/3$ for the relatively low Reynolds numbers. For a relatively high Reynolds number, it is observed that too large ΔV_l^* in (26) can result in a numerical instability, hence, one may need to increase the value of N_b properly.

For the spheroid, the collocation points are located in a sequence of evenly distributed parallel planes that are perpendicular to the axis of symmetry of the spheroid and their distribution in each plane has the same pattern as for the circular particle (Fig. 1b). We first determine the number of rings in the equatorial plane according to the number of the Eulerian grids within an equatorial radius, as for a spherical particle, and then determine the number of the planes according to the aspect ratio of the spheroid. An example of the node arrangement is shown in Fig. 1d.

2.2.5. Tracking the particle orientation

The position of the particle $\mathbf{X}$ can be determined from the following kinematic equation

$$\frac{\mathrm{d}\mathbf{X}}{\mathrm{d}t} = \mathbf{U}. \tag{34}$$

For the particle of non-symmetric shape, it is necessary to track its orientation. It has been shown that our DLM/FD code can successfully deal with the rotation of a spheroid in Couette flow [33]. In the following, we describe a similar approach for our DF/FD method.

The orientation of a particle is determined from the following equations [34]:

$$\begin{pmatrix} \dot{q}_1 \\ \dot{q}_2 \\ \dot{q}_3 \\ \dot{q}_4 \end{pmatrix} = \frac{1}{2} \begin{pmatrix} q_4 & -q_3 & q_2 & q_1 \\ q_3 & q_4 & -q_1 & q_2 \\ -q_2 & q_1 & q_4 & q_3 \\ -q_1 & -q_2 & -q_3 & q_4 \end{pmatrix} \begin{pmatrix} \omega_x \\ \omega_y \\ \omega_z \\ 0 \end{pmatrix}. \tag{35}$$

In (35), q_1, q_2, q_3, q_4 are the components of a quaternion, which can be defined in terms of the Euler angles:

$$\begin{aligned} q_1 &= \sin(\theta/2)\cos((\phi-\psi)/2),\\ q_2 &= \sin(\theta/2)\sin((\phi-\psi)/2),\\ q_3 &= \cos(\theta/2)\sin((\phi+\psi)/2),\\ q_4 &= \cos(\theta/2)\cos((\phi+\psi)/2). \end{aligned} \tag{36}$$

ω_x, ω_y and ω_z represent the components of the angular velocity measured in a body-fixed frame. The quaternion components are normalized, with $\Sigma_m q_m^2 = 1$. Both a quaternion and Euler angles can describe the relationship between the body-fixed frame and the space-fixed frame, however, the Euler angles themselves can not be determined unambiguously at $sin(\theta) = 0$, and consequently are not employed here. With the quaternion, the coordinate transformation matrix from the space-fixed frame to the body-fixed frame is

$$\mathbf{A} = 2\begin{pmatrix} q_1^2+q_4^2-\frac{1}{2} & q_1q_2+q_3q_4 & q_1q_3-q_2q_4\\ q_1q_2-q_3q_4 & q_2^2+q_4^2-\frac{1}{2} & q_2q_3+q_1q_4\\ q_1q_3+q_2q_4 & q_2q_3-q_1q_4 & q_3^2+q_4^2-\frac{1}{2} \end{pmatrix}. \tag{37}$$

A is an orthogonal matrix, satisfying $\mathbf{A}^{-1} = \mathbf{A}^{\mathrm{T}}$. For the axisymmetric body such as a spheroid, z-axis of a body-fixed frame alone is able to determine the orientation of the body, and that is $2(q_1q_3 + q_2q_4, q_2q_3 - q_1q_4, q_3^2 + q_4^2 - \frac{1}{2})$ in the space-fixed frame.

In our implementation, the fluid velocity $\mathbf{u}$, the particle translational velocity $\mathbf{U}$ and the body-force $\boldsymbol{\lambda}$ are measured in the space-fixed frame, while the particle angular velocity $\boldsymbol{\omega}_s$ and the position vector $\mathbf{r}$ are measured in the body-fixed frame. Therefore, three coordinate transformations are required in the solution of the particle subproblem (28)–(32): one is for determining P in the space-fixed frame: $\mathbf{x} = \mathbf{X} + \mathbf{A}^{-1}\cdot\mathbf{r}$; one is to transform $\left(\frac{\mathbf{u}^*}{\Delta t} - \boldsymbol{\lambda}^n\right)$ in (29) from the space-fixed frame to the body-fixed frame; and the last one is to transform $\boldsymbol{\omega}_s^{n+1}\times\mathbf{r}$ in (31) from the body-fixed frame to the space-fixed frame.

3. Numerical experiments

3.1. Flow over a fixed cylinder

We first validate the method in case of prescribed velocity on the immersed boundary via the benchmark problem of the flow over a fixed cylinder, considering that our method in this case differs from any previously reported immersed boundary method in the implementation details regarding the solution of the body-force. In addition, through this example, we aim to demonstrate that for the case of the singular body-force being distributed only on the boundary the discrete nominal support area for the body-force is not important to the results and the Lagrangian nodes should also be retracted a little from the boundary if one wants to use the body-force to calculate the hydrodynamic force on the body.

For the particulate flows, we distribute the Lagrangian nodes over the particle domain to avoid the explicit calculation of the unsteady terms in the expressions of the hydrodynamic force and torque. For the case of prescribed velocity on the boundary, there is no clear advantage from the additional rigidity constraint for the fictitious domain, therefore we distribute the nodes only on the boundary to enforce the no-slip condition. In this case, the dimensionless hydrodynamic force is determined from

$$\mathbf{F}^{\mathrm{H}} = -\int_P \boldsymbol{\lambda}\,\mathrm{d}\mathbf{x} + \int_P \frac{\mathrm{d}\mathbf{u}}{\mathrm{d}t}\mathrm{d}\mathbf{x}. \tag{38}$$

For the stationary cylinder, the contribution of the unsteady term in (38) is expected to be small, since the velocity of the fluid inside the cylinder boundary should vanish theoretically due to the zero velocity on the boundary. Indeed, we found that its contribution to the total hydrodynamic force calculated using the velocities on the Cartesian grids inside the boundary was less than 1%, which is not zero because of the use of non-boundary-fitted mesh. The body-force is defined on the volumeless boundary, but we assume that the body-force at a Lagrangian node has a nominal support area ΔV, which is used to transfer the body-force

from the node to the neighboring Cartesian nodes via (26) and to integrate the body-force term in (38) via $\int_P \boldsymbol{\lambda} d\mathbf{x} = \sum \boldsymbol{\lambda}_i \Delta V$.

It is necessary to examine the effect of the nominal support area ΔV on the results. The test problem is the flow over a fixed cylinder located in a channel with the width being 32 cylinder diameters (i.e., $W/D = 32$) at $Re = 100$. A homogeneous normal boundary condition is imposed for the velocities at the outlet of the flow, and the dimensionless velocities on the other boundaries are set to be unity. Further increase in the channel width was observed to has an insignificant effect on the drag force exerted on the cylinder. The Eulerian mesh size is $h = a/16$, and the spacing of the Lagrangian nodes is $\Delta l = 1.45h$. $\Delta t = 0.01$. Fig. 2 shows the comparison of the time developments of the drag and lift coefficients for $\Delta V = \Delta l h$ and $\Delta V = \Delta l h/2$. The results indicate that the value of ΔV has a marginal effect on the hydrodynamic force on the cylinder. This is not surprising since $\boldsymbol{\lambda}_i \Delta V$ is introduced into the momentum as a whole to enforce the constraint of the given velocity on the boundary, and a smaller $\boldsymbol{\lambda}_i$ is resulted if a larger ΔV is used. However, a numerical instability was observed for a too large $\Delta V = 2\Delta l h$. One could simply set $\Delta V = h^2$ (h^3 for 3D) for all cases, irrespective of the spacing of the Lagrangian nodes.

Our drag and lift coefficients and Strouhal numbers are compared to other results in the literature in Table 1. The effect of the spacing of the Lagrangian nodes on the results is negligible, as seen from the comparison between $\Delta l = 1.45$ h and $\Delta l = 1.2$ h. Lai and Peskin [9] and Uhlmann [11] also used the immersed boundary method with the forcing points defined on the boundary (but using Peskin's δ-function) and calculated the drag force using the body-force, and we can see that our drag and lift coefficients are close to theirs. It has been observed that the value of the drag coefficient obtained in this way is too large compared to most results in the literature (e.g., Liu et al. with a boundary-fitted method and Le et al. with an immersed interface method), and the reason remains unclear. We think that one factor is related to the calculation of the hydrodynamic force using (38). Eq. (38) requires the support area for the body-force to be distributed inside the boundary, however, the body-force affects the velocities on both sides of the boundary via the discrete δ-function, and consequently the support area is actually distributed across the boundary rather than inside the boundary. As a result, the Lagrangian nodes should be retracted a little from the boundary in order to obtain a correct hydrodynamic force from (38). Such a treatment is of course not necessary if the hydrodynamic force is not of interest, or it is obtained by computing the stress on the boundary. The result for the retraction distance $\Delta a = h/2$ is presented in Table 1, and one can see that the drag and lift coefficients are indeed reduced.

It is hard to assess the accuracy of a method from the comparison to the results in the literature on the flow over a cylinder in a wide channel, due to the lack of highly accurate solutions and the difference in the geometry and boundary condition treatment. Therefore, we present our spectral-element (SPE) results on the drag coefficients for a channel with the finite width of $W/D = 4$, and then compare our DF/FD results to them in

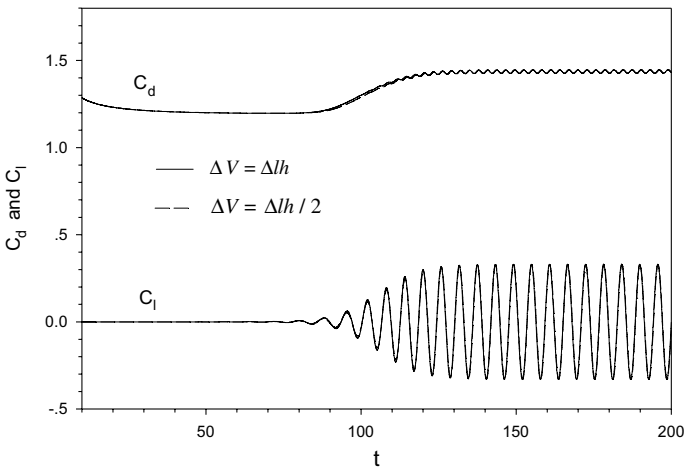

Fig. 2. Comparison of the time developments of the drag and lift coefficients for the flow over a cylinder at two different nominal support areas for the body-force. $Re = 100$, $W/D = 32$, $h = D/16$, $\Delta t = 0.01$.

Table 1
Comparison of the drag and lift coefficients for the flow over a cylinder in a wide channel at $Re = 100$

	C_d	C_l	St
Present results; $\Delta l = 1.45h$	1.432 ± 0.010	± 0.332	0.171
Present results; $\Delta l = 1.2h$	1.431 ± 0.010	± 0.331	0.171
Present results; $\Delta a = h/2$	1.394 ± 0.009	± 0.316	0.174
Uhlmann [11]	1.453 ± 0.011	± 0.339	0.169
Lai and Peskin [9]	$1.447\pm$	± 0.330	0.165
Liu et al. [35]	1.350 ± 0.012	± 0.339	0.165
Le et al. [15]	1.37 ± 0.009	± 0.323	0.160

order to assess the accuracy of the method and further support the argument that the Lagrangian nodes should be retracted to obtain a more accurate hydrodynamic force. For our spectral-element code, the 8th-order Legendre polynomial is used as the shape function for both velocity and pressure. The same projection scheme as used for the present DF/FD method [21] is employed for the temporal discretization. The reader is referred to [36,37] for the details on the SPE method. The spectral-element mesh in the vicinity of the cylinder is shown in Fig. 3. Both SPE and DF/FD results are presented in Table 2. Unfortunately, we observed the spurious pressure oscillation in our SPE simulations for $Re = 100$ and 200, thus, the drag coefficients at these two Reynolds numbers are not provided. We are not clear about the reason for the spurious pressure oscillation and postpone the improvement on the SPE code for high Re to a future study.

From Table 2, the relative errors in the drag coefficients C_d obtained using the present DF/FD method with $h = a/8$ and no retraction (M1) for $Re = 0.5$–40 are 3.3–3.8% compared to the SPE results. The relative errors are reduced to 0.18–0.23% by just retracting the points $h/4$ distance from the cylinder boundary (M1c1), which are smaller than those (1.5–1.8%) by decreasing the mesh size to $h = a/16$ (M2), and (0.74–0.91%) to $h = a/32$ (M3). The optimal retraction distance Δa for this problem is between $h/5$ and $h/4$, being shifted closer to $h/5$ as h is decreased to $h = a/32$. The maximal relative error for the case of M3c2 ($h = a/32$, $\Delta a = h/5$) is below 0.07%.

The drag coefficients for $Re = 100$ and 200 in Table 2 are the average values. In case of M3c2, $(C_d, C_l, St) = (2.024 \pm 0.017, \pm 0.5849, 0.230)$ for $Re = 100$ and $(C_d, C_l, St) = (1.866 \pm 0.076, \pm 1.058, 0.245)$ for $Re = 200$.

3.2. Sedimentation of a circular particle in a channel

Throughout the present study, the results are computed and presented in the dimensionless form, thus we need to define the characteristic velocity and length for each case. For low Reynolds numbers, there exists an analytical expression for the drag force on a circular particle settling in a channel at the velocity U:

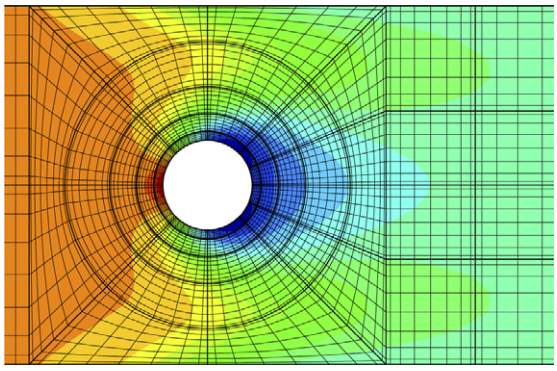

Fig. 3. Spectral-element (SPE) mesh in the vicinity of the cylinder for the flow over a stationary cylinder in a channel. The pressure contours for $Re = 40$ are also plotted.

Table 2
Drag coefficients C_d for the flow over a cylinder in a channel of $W/D = 4$ at different Re obtained using the spectral-element method and the DF/FD method with different mesh sizes: $M1(h = a/8,\ \Delta\ a = 0)$, $M1c1(h = a/8,\ \Delta a = h/4)$, $M2(h = a/16,\ \Delta a = 0)$, $M2c1(h = a/16,\ \Delta a = h/4)$, $M2c2(h = a/16,\ \Delta a = h/5)$, $M3(h = a/32,\ \Delta a = 0)$ and $M3c2(h = a/32,\ \Delta a = h/5)$

Re	SPE	M1	M1c1	M2	M2c1	M2c2	M3	M3c2
0.5	87.95	91.28	87.78	89.51	87.76	88.12	88.75	87.99
1	44.16	45.82	44.07	44.94	44.06	44.25	44.56	44.19
5	9.754	10.10	9.733	9.915	9.733	9.772	9.837	9.759
10	5.749	5.942	5.736	5.839	5.738	5.759	5.795	5.751
20	3.756	3.882	3.748	3.813	3.749	3.762	3.785	3.756
40	2.682	2.778	2.677	2.723	2.676	2.682	2.702	2.681
100		2.119	2.007	2.059	2.021	2.030	2.042	2.024
200		1.964	1.785	1.905	1.862	1.873	1.888	1.866

$$F_d = 4\pi K \mu U, \tag{39}$$

where K is a constant related to the effect of the channel width on the drag force and can be expressed in terms of the ratio of the channel width to the particle diameter W^* (i.e., W/D) [38]:

$$K = \frac{1}{\ln W^* - 0.9157 + 1.7244/(W^*)^2 - 1.7302/(W^*)^4 + 2.4056/(W^*)^6 - 4.5913/(W^*)^8}. \tag{40}$$

By taking the characteristic velocity U_c as

$$U_c = \frac{\frac{\pi D^2}{4}(\rho_s - \rho_f)g}{4\pi K \mu} = \frac{D^2}{16 K \mu}(\rho_s - \rho_f)g, \tag{41}$$

the dimensionless terminal settling velocity is expected to be unity. The characteristic length is the particle diameter. We take the Reynolds number Re and the density ratio ρ_r as the independent dimensionless control parameters, and then the Froude number Fr is not independent and can be expressed in terms of Re and ρ_r as follows:

$$Fr = \frac{16K}{(\rho_r - 1)Re}. \tag{42}$$

For the case of a relatively strong inertial effect, we take the characteristic velocity U_c as

$$U_c = \sqrt{\frac{\frac{\pi D^2}{4}(\rho_s - \rho_f)g}{\frac{\rho_f D}{2}}} = \sqrt{\frac{\pi D}{2}(\rho_r - 1)g}, \tag{43}$$

so that one can conveniently obtain the standard drag coefficient C_d from $C_d = 1/(U_T^*)^2$, here U_T^* being the computed dimensionless terminal settling velocity. Another advantage of this non-dimensionlization scheme is that U_T^* is always not far away from unity. The Froude number in this case becomes

$$Fr = \frac{2}{\pi(\rho_r - 1)}. \tag{44}$$

We will consider the sedimentation of a circular particle in a vertical channel at $Re = 0.1$ and 200, respectively. The characteristic velocity is defined by (41) for $Re = 0.1$ and (43) for $Re = 200$. The particle is released at the center of the channel. Fig. 4a shows the time developments of the settling velocities at $\Delta t = 0.001$,0.0005 and 0.0002 for $Re = 0.1$, $W/D = 4$ and $h = a/8$, and the results exhibit a satisfactory time-step independence. Using $\Delta t = 0.001$, the simulation of the acceleration process from zero velocity to the steady-state velocity only requires less than 100 time steps. Fig. 4b shows the time developments of the settling velocities at different numbers of Lagrangian nodes: $N_a = 5$,6 and 7. We see that the effect of the number of Lagrangian nodes is insignificant, and the settling velocity decreases slightly with increasing number of nodes for a given h.

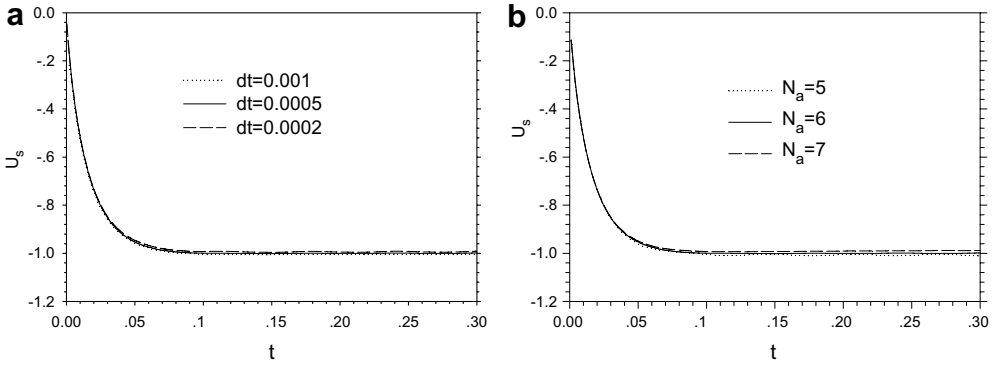

Fig. 4. Time developments of the settling velocities of a circular particle in a vertical channel of $W/D = 4$ at (a) different time-steps and (b) different numbers of Lagrangian nodes. $Re = 0.1$, $\rho_r = 1.2$, $h = a/8$, $\Delta a = h/3$. For (a) $N_a = 6$. For (b) $\Delta t = 0.0005$.

Figs. 5a and 5b plot the time developments of the settling velocities at different retraction distances for $h = a/8$ and $a/16$, respectively. For $h = a/8$, the optimal Δa is around $h/3$, and the maximal relative errors in the terminal settling velocities for $h/4 \leqslant \Delta a \leqslant h/2$ are below 1.5% compared to the analytical solution. This optimal value of Δa is larger than that for the body-force being located only on the boundary (recall that it is around $h/4$ for $h = a/8$). The optimal $\Delta a/h$ is also reduced as h is decreased in the present case, being around 1/4 for $h = a/16$, as shown in Fig. 5b.

The results on the effect of the retraction on the sedimentation velocity at $W/D = 16$ and at $Re = 200$ are presented in Fig. 6ab. It is seen that the effect becomes more insignificant for a wider channel or a higher Reynolds number. There is no oscillation in the settling velocities for $Re = 200$ in Fig. 6b, because the expected vortex shedding has not taken place by the end of the simulation.

For a non-symmetric particle, the collocation points change positions as the particle rotates. However, for a circular or spherical particle, we may or may not let the points move with the rotation of the particle. The trajectories of a circular particle released at the lateral position of one particle diameter away from the wall at $Re = 200$ obtained with and without the rotation of the points are compared in Fig. 7, and one can see that the difference is insignificant. Hence, we will not consider the rotation of the collocation points for the spherical particle below. The result obtained using the DLM/FD code with the collocation-point method and the same node arrangement is also compared in Fig. 7. It is encouraging to find that the results from the two methods are in excellent agreement with each other, as actually for all cases we tested, including the example of the migration velocity of a sphere in a pipe, as shown in Fig. 10. Therefore, our DF/FD method is equally accurate as the DLM/FD method.

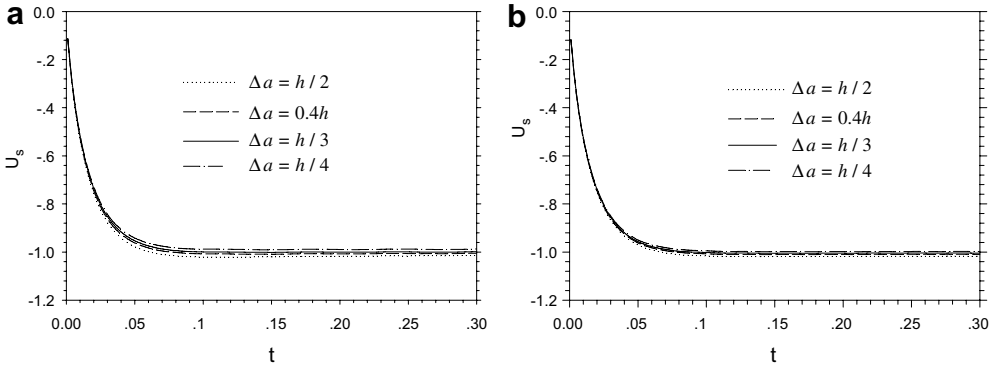

Fig. 5. Time developments of the settling velocities of a circular particle in a vertical channel of $W/D = 4$ at different retraction distances for (a) $h = a/8$, $N_a = 6$ and (b) $h = a/16$, $N_a = 12$. $Re = 0.1$, $\rho_r = 1.2$, $\Delta t = 0.0005$.

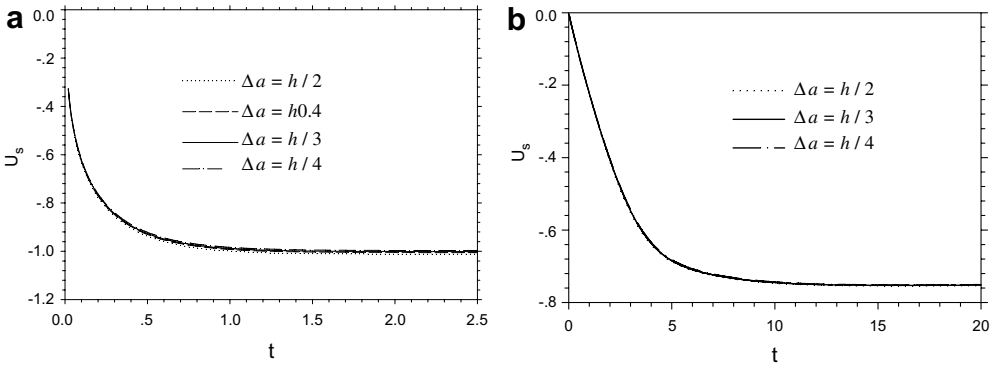

Fig. 6. Time developments of the settling velocities of a circular particle in a vertical channel at different retraction distances for (a) $W/D = 16$, $Re = 0.1$, $\rho_r = 1.2$, $h = a/8$, $N_a = 6$, $\Delta t = 0.005$, and (b) $W/D = 4$, $Re = 200$, $\rho_r = 1.1$, $h = a/16$, $N_a = 12$, $\Delta t = 0.01$.

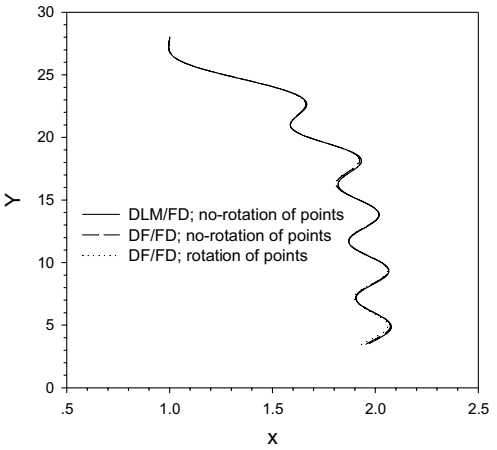

Fig. 7. Comparison of the trajectories of a circular particle in a vertical channel of $W/D = 4$ obtained with different schemes. $Re = 200$, $\rho_r = 1.1$, $h = a/16$, $N_a = 12$, $\Delta a = h/3$, $\Delta t = 0.01$.

3.3. Sedimentation of a spherical particle in a vertical pipe

We take the sphere diameter as the characteristic length, and define the characteristic velocity U_c by

$$U_c = \sqrt{\frac{8a}{3}(\rho_r - 1)g} \tag{45}$$

so that

$$C_D = \frac{\frac{4\pi a^3}{3}(\rho_s - \rho_f)g}{\frac{\pi a^2 \rho_f U_T^2}{2}} = \frac{U_c^2}{U_T^2} = \frac{1}{(U_T^*)^2}, \tag{46}$$

and

$$N_D = \frac{4(\rho_s - \rho_f)g(2a)^3\rho_f}{3\mu^2} = Re^2, \tag{47}$$

where U_T and U_T^* are the dimensional and dimensionless terminal sedimenting velocity, respectively, and N_D is sometimes called the "Best number" [39]. The Froude number in this case becomes

$$Fr = \frac{3}{4(\rho_r - 1)}. \tag{48}$$

The Reynolds number Re_T, which is based on the terminal settling velocity, can be calculated by using

$$Re_T = U_T^* Re. \tag{49}$$

The fluid-flow problem is posed on a cuboid (rectangular box). An additional body-force is introduced to enforce the Dirichlet boundary condition on the pipe wall with the new DF/FD scheme instead of the DLM/FD method. The pipe-particle diameter ratio is 5, and the size of the computational domain is typically $5D \times 5D \times 25D$. To mimic an infinitely long pipe, we shift the flow fields and the particle position upwards one mesh distance once the particle falls below a vertical position that is $6D$ higher than the bottom inlet so that the computational domain looks like moving with the particle.

We have examined earlier the effects of the number of the collocation points and the retraction distance on the determination of the settling velocity of a circular particle at the low Reynolds numbers in two dimensions. The qualitatively same results were observed in our numerical tests on the sedimentation of the spherical particle in a vertical pipe at the low Reynolds numbers, and $\Delta a = h/3$ is also good in this case. We now focus on the computations at relatively high Reynolds numbers. Fig. 8 illustrates that the pattern of the node arrangement does not affect significantly the settling velocity of a spherical particle for a given h at $Re = 100$. As mentioned earlier, too large control volume for each collocation point (say, $\Delta V^* > 2$) would result in the numerical instability at a relatively high Reynold number, so a high N_b is required for a lower N_a.

Fig. 9a shows the time developments of the settling velocity at different Re. The particle is released at the axis of the pipe. For $Re = 300$, the vortex shedding takes place and the freely-falling particle will depart from the tube axis. The result for a sphere at $Re = 300$ with the lateral velocity constrained to vanish is also plotted in Fig. 9a. Our results on Re_T vs. $N_D^{1/3}$ are compared to the experimental data [39] for a sphere fixed on the axis in Fig. 9b. One can see a good agreement for $Re_T < 100$, and an appreciable discrepancy for $Re_T > 100$. Our Re_T is smaller than the experimental one at the same N_D (or Re) for $Re_T > 100$, indicating that the drag coefficient is overestimated by our calculation. Recalling that our drag coefficient with $\Delta a = h/2$ at $Re = 100$ is still larger than Liu et al.'s and Le et al.'s in the problem of the flow over a fixed cylinder discussed earlier, it seems that our DF/FD method is not suited to the simulation of the particle sedimentation for $Re > 100$. A possible reason for the poor accuracy at high Re is that the strong discontinuity of some quantities such as the velocity gradient across the surface is not directly considered for the discretization of the differential operators at the Eulerian nodes in the immediate vicinity of the boundary in our method, unlike the sharp interface method [2] or immersed interface method [15]. Nevertheless, it has been shown that the accuracy of our method is satisfactory for relatively low Reynolds numbers, a Re regime in which we are most interested due to the fact that the flows of suspensions of small particles typically occur in this Re regime.

Figs. 8 and 9b indicate that it is better to use a fine mesh for the high Reynolds number simulations. However, because we employ a homogeneous mesh throughout the entire computational domain, the use of a very fine mesh for $R/a = 5$ or the computation for a large R/a is beyond our computational resource.

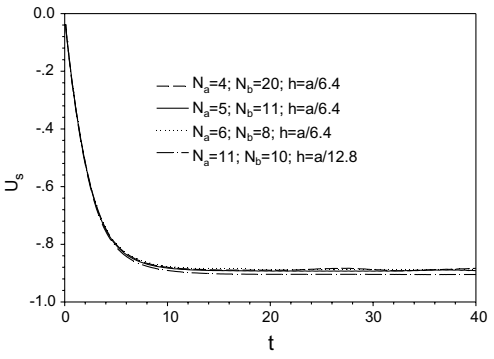

Fig. 8. Effect of the node arrangement on the settling velocity of a sphere in a vertical tube of $R/a = 5$. Re = 100, $\rho_r = 1.1$, $\Delta a = h/3$, $\Delta t = 0.01$.

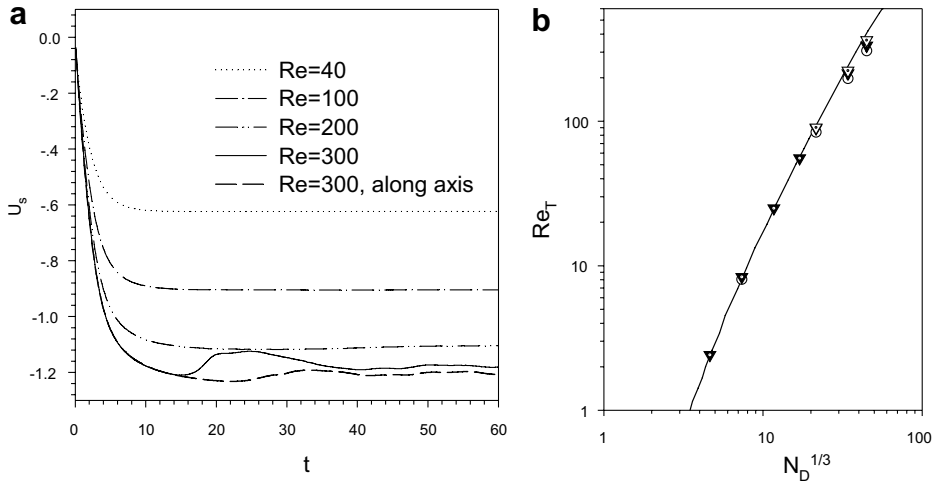

Fig. 9. (a) Time developments of the settling velocity for a sphere in a vertical pipe of $R/a = 5$ at different Re and (b) Re_T vs. $N_D^{1/3}$ for a sphere settling along the axis of the pipe. For (b), solid line: experimental results [39]; solid triangle: DF/FD results with $h = a/6.4$; open triangle: DF/FD results with $h = a/12.8$; open circle: previous DLM/FD results with $h = a/6.4$ [20]. $\rho_r = 1.1$, $\Delta t = 0.01$ and $\Delta a = h/3$ for the DF/FD computations.

3.4. Inertial migration of a sphere in circular Poiseuille flow

For the case of a spherical particle moving in Poiseuille flow, we take the initial maximum velocity of the flow at the centerline of the tube U_m and the particle radius R as the characteristic velocity and length, respectively. The Reynolds number based on them is the tube Reynolds number Re_t. A dimensionless parameter λ_f is defined by [40]

$$\lambda_f = \frac{U_f}{U_m}, \tag{50}$$

where U_f is the Stokes free-fall velocity of a sphere, i.e., $U_f = 4a^2(\rho_s - \rho_f)g/18\mu$. The Froude number for the non-neutrally-buoyant case has the form:

$$Fr = \frac{9\lambda_f}{2(\rho_r - 1)(a/R)^2 Re_t}. \tag{51}$$

The periodic boundary condition is imposed on the streamwise direction, and we fix the dimensionless additional pressure gradient to be $(-4/Re_t)$, the value required for just sustaining the steady circular Poiseuille flow of Newtonian fluids. For a single neutrally-buoyant or slightly denser particle, the flow flux and thereby the tube Reynolds number change only slightly during the simulations.

Fig. 10 displays our results on the radial migration velocities vs. radial position for a neutrally-buoyant sphere at $(Re_t, a/R) = (100, 0.25)$ and a denser sphere in downward Poiseuille flow at $(Re_t, \lambda_f, a/R, \rho_r) = (89.8, 0.0674, 0.09, 1.01)$. Yu et al. [20] investigated numerically the radial migration of a spherical particle in Poiseuille flow using the DLM/FD method, and the results for the corresponding cases are also plotted in Fig. 10 for comparison. Because a different time discretization scheme (without keeping λ^n in the momentum equation) and space scheme (collocation-element) were used for the body-force in Yu et al., there are slight discrepancies between the previous DLM/FD and present DF/FD results, as shown in Fig. 10. When the same discretization schemes are used for the body-force, the results obtained with the DLM/FD and DF/FD methods are in good agreement with each other. For the DLM/FD method, the radial velocity from iteration is of poor quality, being oscillatory with time. By contrast, the solution from the DF/FD method is much smoother, as illustrated in Fig. 10.

From Fig. 10, our migration velocities agree well with the experimental results of Jeffrey and Pearson [40]. The experimental data are scattered due to the difficulty in measuring such a small radial migration velocity compared to the mainstream velocity.

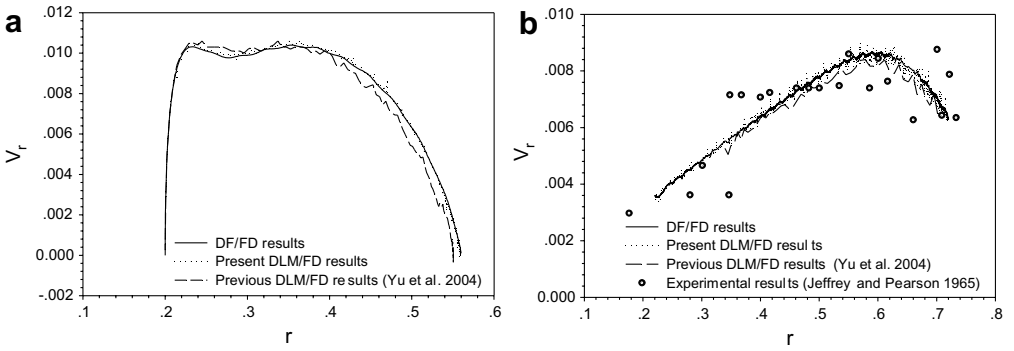

Fig. 10. Radial migration velocities vs. radial position for (a) a neutrally-buoyant sphere at $(Re_t, a/R) = (100, 0.25)$ and (b) a denser sphere in downward Poiseuille flow at $(\mathrm{Re}_t, \lambda_f, a/R, \rho_r) = (89.8, 0.0674, 0.09, 1.01)$. For (a) $h = a/8$, and for (b) $h = a/5.76$. $\Delta t = 0.01$.

Fig. 11 shows the comparison between the results of Pan and Glowinski [41,42] and ours on the migration of a neutrally-buoyant sphere. Pan and Glowinski obtained the results using their finite-element-based DLM/FD code. Dimensional quantities are used in their computations. In the CGS unit system, the density is 1, the fluid viscosity 1, the maximum velocity 20, the radius of the sphere 0.375, the radius of the tube 2.5, and the length of the tube 10. From these dimensional quantities and our definition of the characteristic velocity and length above, we can obtain the dimensionless parameters $(Re_t, a/R) = (50, 0.15)$, and one dimensionless time unit corresponds to 0.125 s. For our computations, $\Delta t = 0.005$, and $h = a/4.8$, which results in the total number of velocity (or pressure) meshes being $64 \times 64 \times 128$ for the entire computational domain. Further decrease in the time step was observed to have an insignificant effect on the results. Veeramani et al. [24] compared their results to those of Pan and Glowinski, and we actually reproduce the data of Pan and Glowinski from [24]. From Fig. 11, one can see that our results are in good agreement with Pan and Glowinski's. Due to the use of a sequence of efficient solvers such as the finite-difference-based projection method for the Navier–Stokes equations, the FFT-based fast solver for the pressure Poisson equation, the ADI scheme for the velocity Helmholtz equation [21], and the present non-iterative scheme for the rigidity constraints for the tube wall and the particle, it takes only about 0.92 s per time-step on a 2.8 GHz INTEL CPU (with the INTEL FORTRAN compiler). The FFT-based fast solver only works for the homogeneous mesh, as in our code, and thus is specifically suited to the problem of particulate flows (suspension) where a homogeneous mesh is usually desirable.

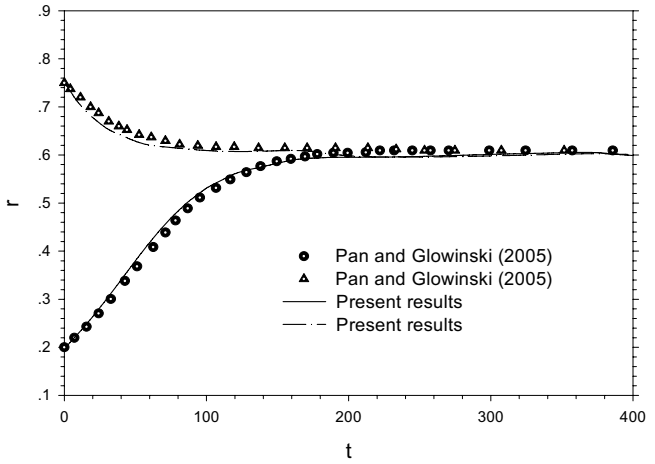

Fig. 11. Time evolution of the radial position of a neutrally-buoyant spherical particle released at $r_0 = 0.2$ and 0.75, respectively, for $(Re_t, a/R) = (50, 0.15)$, as compared to the results of Pan and Glowinski [41]. For our computations, $\Delta t = 0.005$, $h = a/4.8$, $N_a = 4$, $N_b = 8$, and $\Delta a = h/3$.

3.5. Rotation of a neutrally-buoyant sphere in Couette flow

A neutrally-buoyant spherical particle suspended at the center of a Couette cell is considered. The shear-rate is $\dot{\gamma}$, and the cell size is $L \times L \times L$. The characteristic length and velocity are the sphere radius a and $a\dot{\gamma}$, respectively. From (6), one can derive

$$\int_P \boldsymbol{\sigma}\,\mathrm{d}\mathbf{x} = \int_{\partial P} \frac{1}{2}(\mathbf{r}\boldsymbol{\sigma}\cdot\mathbf{n} + \boldsymbol{\sigma}\cdot\mathbf{n}\mathbf{r})\mathrm{d}\mathbf{x} - \int_P \frac{1}{2}\rho_f\left(\mathbf{r}\frac{\mathrm{d}\mathbf{u}}{\mathrm{d}t} + \frac{\mathrm{d}\mathbf{u}}{\mathrm{d}t}\mathbf{r}\right)\mathrm{d}\mathbf{x} + \int_P \frac{1}{2}(\mathbf{r}\boldsymbol{\lambda} + \boldsymbol{\lambda}\mathbf{r})\mathrm{d}\mathbf{x}. \tag{52}$$

Note that $\boldsymbol{\sigma}$ in (52) denotes the stress of the fluid $\boldsymbol{\sigma}_f$, and from the rigidity constraint (7), the stress appearing in the term on the left-hand side of (52) only has the diagonal pressure part, i.e., $\boldsymbol{\sigma} = -p_\mathrm{f}\mathbf{I}$, here p_f being the pressure of the fictitious fluid inside the particle boundary. On the boundary, the stress of the fictitious fluid is equal to the one of the real fluid, thus, the first term on the right-hand side of (52) represents the stresslet $\mathbf{S}^*$. From (52),

$$\mathbf{S}^* = \int_P \frac{1}{2}\rho_f\left(\mathbf{r}\frac{\mathrm{d}\mathbf{u}}{\mathrm{d}t} + \frac{\mathrm{d}\mathbf{u}}{\mathrm{d}t}\mathbf{r}\right)\mathrm{d}\mathbf{x} - \int_P \frac{1}{2}(\mathbf{r}\boldsymbol{\lambda} + \boldsymbol{\lambda}\mathbf{r})\mathrm{d}\mathbf{x} + \int_P -p_\mathrm{f}\mathbf{I}\,\mathrm{d}\mathbf{x}. \tag{53}$$

From the rigidity constraint, for the case of a spherical particle, one can obtain

$$\int_P \frac{1}{2}\rho_f\left(\mathbf{r}\frac{\mathrm{d}\mathbf{u}}{\mathrm{d}t} + \frac{\mathrm{d}\mathbf{u}}{\mathrm{d}t}\mathbf{r}\right)\mathrm{d}\mathbf{x} = \frac{Ma^2}{5\rho_\mathrm{r}}(\boldsymbol{\omega}_s\boldsymbol{\omega}_s - \boldsymbol{\omega}_s^2\mathbf{I}). \tag{54}$$

The last term in (53) is not relevant when we only consider the rheological property of the suspension, i.e., the viscosity and normal stress differences. Therefore, for a freely-rotating spherical particle in Couette flow, we have

$$\frac{\mathbf{S}^*}{V\mu\dot{\gamma}\phi} = \frac{1}{V_\mathrm{p}\mu\dot{\gamma}}\left[\frac{Ma^2}{5\rho_\mathrm{r}}(\boldsymbol{\omega}_s\boldsymbol{\omega}_s - \boldsymbol{\omega}_s^2\mathbf{I}) - \int_P \frac{1}{2}(\mathbf{r}\boldsymbol{\lambda} + \boldsymbol{\lambda}\mathbf{r})\mathrm{d}\mathbf{x}\right], \tag{55}$$

where V, V_p and ϕ are the volume of the Couette cell, the volume of the particle and the particle volume fraction, respectively. For convenience, we define $\mathbf{S} = \frac{\mathbf{S}^*}{V\mu\dot{\gamma}\phi}$. Note that the quantities in (55) are dimensional. In terms of dimensionless quantities (recall that $\boldsymbol{\lambda}$ is scaled as $\rho_f U_\mathrm{c}^2/L_c$), $\mathbf{S}$ can be expressed as

$$\mathbf{S} = \frac{Re}{5}(\boldsymbol{\omega}_s\boldsymbol{\omega}_s - \boldsymbol{\omega}_s^2\mathbf{I}) - \frac{Re}{V_\mathrm{p}^*}\int_P \frac{1}{2}(\mathbf{r}\boldsymbol{\lambda} + \boldsymbol{\lambda}\mathbf{r})\mathrm{d}\mathbf{x}. \tag{56}$$

With the finite-element method, Mikulencak and Morris [43] investigated the free rotation of a spherical particle in a domain bounded with a outer spherical surface of radius R^∞, on which the Dirichlet boundary condition is imposed according to the simple shear flow. For our Couette cell, the periodic boundary condition is imposed on the flow and vorticity directions (see Fig. 13), and only the gradient direction is bounded with two parallel plates on which the Dirichlet boundary condition is imposed. Our results on the angular velocity and stresslet of the particle as a function of Re for $Re \leqslant 10$ at $L/(2a) = 7.25$ are compared to those of Mikulencak and Morris [43] in Fig. 12. In our simulations, we let the computation for each case run until $t = 30$ (i.e., 30 strains), which is long enough to achieve a steady state; we observed that the angular velocity and stresslet have typically converged to the fifth digit at the end of the simulations. One can see that the two results are in good agreement with each other. For the stresslet, we adopt the data of Mikulencak and Morris for $R^\infty/a = 7.25$. We are not clear about the value of R^∞/a for the computation of their angular velocities. The angular velocity is smaller for a bigger bounding domain at a high Reynolds number [43], hence, the difference in the angular velocity between two results at $Re = 10$ in Fig. 12a could be reduced if they used a large R^∞. Nevertheless, the relative difference at $Re = 10$ is actually not much, being around 2.4% (the angular velocity being 4.33 and 4.23, respectively). For our computations, we use $N_b = 8$ and $\Delta a = h/3$ for $Re < 4$, but $N_b = 10$ and $\Delta a = 0.4h$ for $Re \geqslant 4$. The reason why we choose $N_b = 10$ for $Re \geqslant 4$ is that the computation with $N_b = 8$ becomes unstable as Re is increased to this level. We accordingly increase the value of Δa since in this way the calculated stresslets for two sets of collocation points are found to match better at $Re = 1$. The effect of the node arrangement (e.g., N_b and Δa) on the angular velocity is found insignificant.

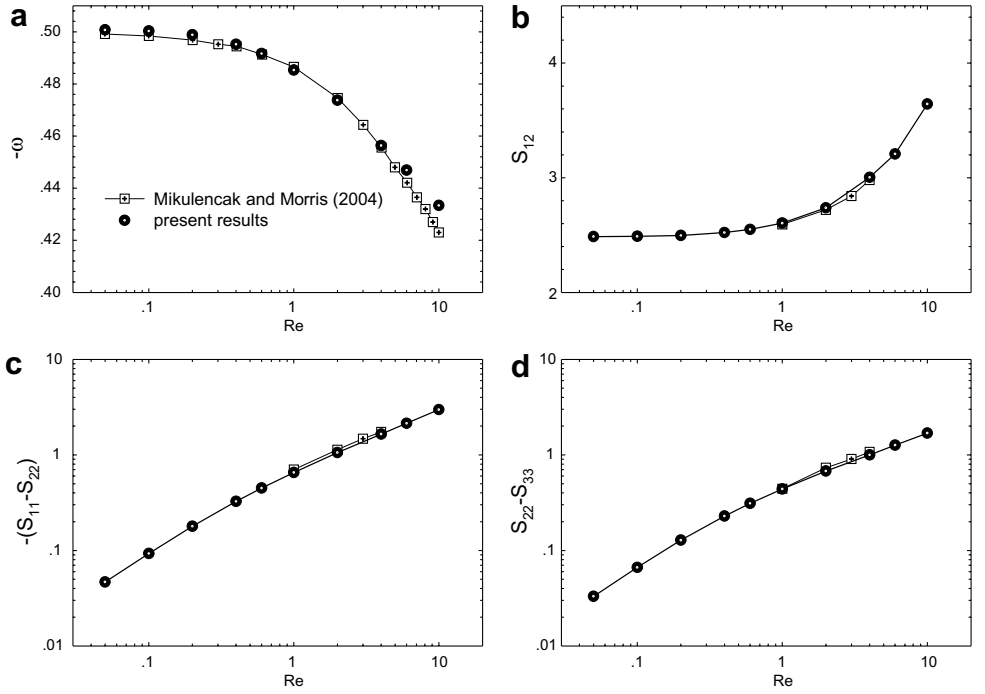

Fig. 12. Angular velocity and stresslet as a function of Re for a neutrally-buoyant spherical particle suspended at the center of a cubic Couette cell. $L/(2a) = 7.25$, $\rho_r = 1.0$, $h = a/(128/14.5) \approx a/8.83$, $N_a = 8$. For $Re < 4$, $N_b = 8$ and $\Delta a = h/3$; for $Re \geqslant 4$, $N_b = 10$ and $\Delta a = 0.4$ h.

3.6. Rotation of a prolate spheroid in Couette flow

The schematic diagram of a spheroid rotating in Couette flow is shown in Fig. 13. The computational domain is a box with the size of $L_1 \times L_2 \times L_3$. Periodic boundary conditions are introduced in the streamwise(X) and spanwise(Z) directions. $\mathbf{p}$ is the unit vector along the symmetric axis of the spheroid. Define θ as the angle between $\mathbf{p}$ and the vorticity(Z)-axis, and φ as the angle between the projection of $\mathbf{p}$ on the (X, Y)-plane and the Y-axis, so that

$$\begin{aligned} p_x &= \sin\theta \sin\varphi, \\ p_y &= \sin\theta \cos\varphi, \\ p_z &= \cos\theta. \end{aligned} \tag{57}$$

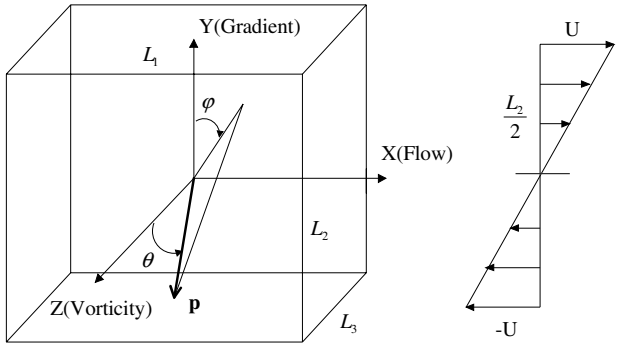

Fig. 13. Schematic diagram of a spheroid rotating in Couette flow. The computational domain is a box with the size of $L_1 \times L_2 \times L_3$. Periodic boundary conditions are introduced in the streamwise(X) and spanwise(Z) directions.

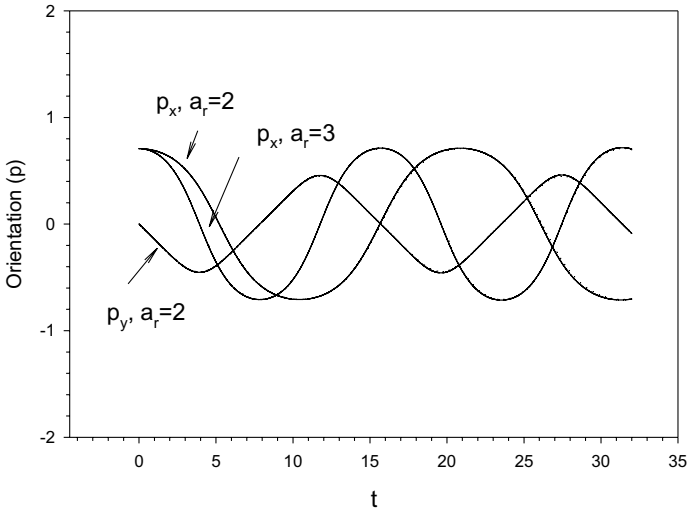

Fig. 14. Comparison between the calculated orientational orbit and the analytical Jeffery orbit for a prolate spheroid in simple shear flow at a low Reynolds number. Solid lines: our results; dotted lines: analytical results, the two being in excellent agreement.

We consider the orientation of a neutrally-buoyant prolate spheroid of the symmetry axis length $2a$ and the equatorial diameter $2b$ during its free rotation in the flow. It is known that the orientation of a spheroid in a simple shear flow of shear-rate $\dot{\gamma}$ obeys the Jeffery orbit [44]:

$$\tan\varphi = a_r \tan(\omega t + k'), \tag{58}$$

$$\tan\theta = \frac{Ca_r}{\sqrt{a_r^2\cos^2\varphi + \sin^2\varphi}}, \tag{59}$$

where a_r is the aspect ratio of the spheroid (i.e., $a_r = a/b$), $\omega = 2\pi/T$, T being the orbit period $\frac{2\pi}{\dot{\gamma}}\left(a_r + \frac{1}{a_r}\right)$, and the constants k' and C are determined from the initial orientation φ_0 and θ_0.

We take $2a$ and $2a\dot{\gamma}$ as the characteristic velocity and length, respectively. For our computations, $Re = 0.1$, $\rho_r = 1.0$, $h = b/6.4$, $\Delta t = 0.001$, $\varphi_0 = \pi/2$ and $\theta_0 = \pi/4$. We set $L_1/(2a) = L_3/(2a) = 2.5$, and $L_2/(2a) = 2.5$ for $a_r = 2$ and 5.0 for $a_r = 3$. The comparison between the calculated orientational orbits and the analytical Jeffery orbits is shown in Fig. 14. The two results are in remarkably good agreement with each other.

4. Conclusions

We have presented the direct-forcing fictitious domain (DF/FD) method for the simulation of particulate flows. The new method is a non-Lagrange-multiplier version of our previous DLM/FD code and is obtained by employing a discrete δ-function in the form of bi(tri-) function to transfer explicitly quantities between the Eulerian and Lagrangian nodes, as in the immersed boundary method. Our method in case of a prescribed velocity on the boundary is verified via the comparison to the benchmark results on the flow over a fixed cylinder in a wide channel and to our spectral-element results for a channel with the width of four cylinder diameters. It is shown that for the case of the body-force distributed only on the boundary the discrete nominal support area for the body-force is not important to the results and the Lagrangian nodes should be retracted a little from the boundary for the calculation of the hydrodynamic force on the body using the body-force. Our new method for the case of the particulate flows is validated through various typical flow situations, including the sedimentation of a circular particle in a vertical channel, the sedimentation of a sphere in a vertical pipe, the inertial migration of a sphere in circular Poiseuille flow, the behavior of a neutrally-buoyant sphere in Couette flow, and the rotation of a prolate spheroid in Couette flow. The new DF/FD method is shown to be equally accurate as the DLM/FD method. Due to the use of the collocation-point approach for the rigidity constraint and the integration over the particle domain, the Lagrangian nodes should be

retracted a little from the particle boundary. In addition, it is shown that there is no significant difference between the unsteady sedimentation results obtained with and without rotation of the Lagrangian nodes.

Unlike the DF/IB method for the particulate flows proposed by Uhlmann [11], our body-force is distributed over the particle inner domain for the rigid-body motion constraint in order to overcome the difficulty in dealing with the nearly neutrally-buoyant case. However, for the case of large ρ_r, the body-force being located only on the surface might be a better choice, since fewer Lagrangian nodes are required.

Only the motion of one particle is considered for the validation of the method. The reader is referred to [7,21,22] for the collision model and successful applications of our DLM/FD method in the many-particle case.

Acknowledgements

The authors would like to acknowledge the support of National Natural Science Foundation of China (Grant Nos.: 10472104 and 10602051), and thank the anonymous referees for helpful suggestions.

References

[1] R. Mittal, G. Iaccarino, Immersed boundary methods, Annu. Rev. Fluid Mech. 37 (2005) 239–261.
[2] S. Marella, S. Krishnan, H. Liu, H.S. Udaykumar, Sharp interface Cartesian grid method I: an easily implemented technique for 3D moving boundary computations, J. Comput. Phys. 210 (2005) 1–31.
[3] R. Glowinski, T-W. Pan, J. Périaux, A fictitious domain method for Dirichlet problems and applications, Comp. Meth. Appl. Mech. Eng. 111 (1994) 283–303.
[4] F. Bertrand, P.A. Tanguy, F. Thibault, A three-dimensional fictitious domain method for incompressible fluid flow problems, Int. J. Numer. Meth. Fluids 25 (1997) 719–736.
[5] R. Glowinski, T.-W. Pan, T.I. Hesla, D.D. Joseph, A distributed Lagrange multiplier/fictitious domain method for particulate flows, Int. J. Multiphase Flow 25 (1999) 755–794.
[6] R. Glowinski, T.-W. Pan, T.I. Hesla, D.D. Joseph, J. Periaux, A fictitious domain approach to the direct numerical simulation of incompressible viscous flow past moving rigid bodies: application to particulate flow, J. Comput. Phys. 169 (2001) 363–426.
[7] Z. Yu, X. Shao, A. Wachs, A fictitious domain method for particulate flows with heat transfer, J. Comput. Phys. 217 (2006) 424–452.
[8] C.S. Peskin, Numerical analysis of blood flow in the heart, J. Comput. Phys. 25 (1977) 220–252.
[9] M.-C. Lai, C. Peskin, An immersed boundary method with formal second-order accuracy and reduced numerical viscosity, J. Comput. Phys. 160 (2000) 705–719.
[10] K. Höfler, S. Schwarzer, Navier–Stokes simulation with constraint forces: finite-difference method for particle-laden flows and complex geometries, Phys. Rev. E 61 (2000) 7146–7160.
[11] M. Uhlmann, An immersed boundary method with direct forcing for the simulation of particulate flows, J. Comput. Phys. 209 (2005) 448–476.
[12] J. Yang, E. Balaras, An embedded-boundary formulation for large-eddy simulation of turbulent flows interacting with moving boundaries, J. Comput. Phys. 215 (2006) 12–40.
[13] D. Kim, H. Choi, Immersed boundary method for flow around an arbitrarily moving body, J. Comput. Phys. 212 (2006) 662–680.
[14] E.A. Fadlun, R. Verzicco, P. Orlandi, J. Mohd-Yusof, Combined immersed-boundary finite-difference methods for three-dimensional complex flow simulations, J. Comput. Phys. 161 (2000).
[15] D.V. Le, B.C. Khoo, J. Peraire, An immersed interface method for viscous incompressible flows involving rigid and flexible boundaries, J. Comput. Phys. 220 (2006) 109–138.
[16] S. Xu, Z.J. Wang, An immersed interface method for simulating the interaction of a fluid with moving boundaries, J. Comput. Phys. 216 (2006) 454–493.
[17] M. Kang, R.P. Fedkiw, X.-D. Liu, A boundary condition capturing method for multiphase incompressible flow, J. Sci. Comput. 15 (2000) 323–360.
[18] W.R. Hwang, M.A. Hulsen, H.E.H. Meijer, Direct simulations of particle suspensions in a viscoelastic fluid in sliding bi-periodic frames, J. Non-Newtonian Fluid Mech. 121 (2004) 15–33.
[19] Z. Yu, N. Phan-Thien, Y. Fan, R.I. Tanner, Viscoelastic mobility problem of a system of particles, J. Non-Newtonian Fluid Mech. 104 (2002) 87–124.
[20] Z. Yu, N. Phan-Thien, R.I. Tanner, Dynamical simulation of sphere motion in a vertical tube, J. Fluid Mech. 518 (2004) 61–93.
[21] Z. Yu, A. Wachs, Y. Peysson, Numerical simulation of particle sedimentation in shear-thinning fluids with a fictitious domain method, J. Non-Newtonian Fluid Mech. 136 (2006) 126–139.
[22] Z. Yu, A. Wachs, A fictitious domain method for dynamic simulation of particle sedimentation in Bingham fluids, J. Non-Newtonian Fluid Mech. 145 (2007) 78–91.
[23] N. Sharma, N.A. Patankar, A fast computation technique for the direct numerical simulation of rigid particulate flows, J. Comput. Phys. 205 (2005) 439–457.

[24] C. Veeramani, P.D. Minev, K. Nandakumar, A fictitious domain formulation for flows with rigid particles: a non-Lagrange multiplier version, J. Comput. Phys. (2006), doi:10.1016/j.jcp.2006.10.028.
[25] C. Diaz-Goano, P. Minev, K. Nandakumar, A fictitious domain/finite element method for particulate flows, J. Comput. Phys. 192 (2003) 105–123.
[26] Z. Yu, A DLM/FD method for fluid/flexible-body interactions, J. Comput. Phys. 207 (2005) 1–27.
[27] X. Shi, N. Phan-Thien, Distributed Lagrange multiplier/fictitious domain method in the framework of lattice Boltzmann method for fluid–structure interactions, J. Comput. Phys. 206 (2005) 81–94.
[28] C.S. Peskin, The immersed boundary method, Acta Numer. (2002) 1–39.
[29] E.M. Saiki, S. Biringen, Numerical simulation of a cylinder in uniform flow: application of a virtual boundary method, J. Comput. Phys. 123 (1996) 450–465.
[30] S.-W. Su, M.-C. Lai, C.-A. Lin, An immersed boundary technique for simulating complex flows with rigid boundary, Comp. Fluids 36 (2007) 313–324.
[31] A.J.C. Ladd, R. Verberg, Lattice-Boltzmann simulations of particle-fluid suspensions, J. Stat. Phys. 104 (2001) 1191–1251.
[32] M.Uhlmann, New Results on the Simulation of Particulate Flows, Technical Report No. 1038, CIEMAT, Madrid, Spain, 2003, ISSN 1135-9420.
[33] Z. Yu, Dynamic Simulation of Particulate Flows with the DLM Method, Ph.D. Thesis, University of Sydney, 2003.
[34] D.C. Rapaport, The Art of Molecular Dynamics Simulation, Cambridge University Press, 1995.
[35] C. Liu, X. Zheng, C. Sung, Preconditioned multigrid methods for unsteady incompressible flows, J. Comput. Phys. 139 (1998) 35–57.
[36] C. Canuto, M.H. Hussaini, A. Quarteroni, T.A. Zang, Spectral Methods in Fluid Dynamics, Springer-Verlag, New York, 1988.
[37] A.T. Patera, A spectral element method for fluid dynamics: laminar flow in a channel expansion, J. Comput. Phys. 54 (1984) 468–488.
[38] J. Happel, H. Brenner, Low Reynolds Number Hydrodynamics, Prentice-Hall, New York, 1965.
[39] R. Clift, J.R Grace, M.E Weber, Bubbles, Drops, and Particles, Academic Press, 1978.
[40] R.C. Jeffrey, J.R. Pearson, Particle motion in laminar vertical tube flow, J. Fluid Mech. 22 (1965) 721–735.
[41] T.-W. Pan, R. Glowinski, Direct simulation of the motion of neutrally buoyant balls in a three-dimensional Poiseuilles flow, C.R. Mec. 333 (2005) 884.
[42] B. Yang, J. Wang, D. Joseph, H. Hu, T. Pan, R. Glowinski, Migration of a sphere in a tube flow, J. Fluid Mech. 540 (2005) 109–131.
[43] D.R. Mikulencak, J.F. Morris, Stationary shear flow around fixed and free bodies at finite Reynolds number, J. Fluid Mech. 520 (2004) 215–242.
[44] G.B. Jeffery, The motion of ellipsoidal particles immersed in a viscous fluid, Proc. R. Soc. London A 102 (1922) 161–179.